

Evolution and Mass Dependence of UV-to-near-IR Color Gradients up to $z = 2.5$ from HST+JWST

M. Martorano¹, A. van der Wel¹, A. Gebek¹, M. Baes¹, E. F. Bell², G. Brammer³, S. E. Meidt¹, A. Nersesian^{4,1}, K. Whitaker^{3,5}, and S. Wuyts⁶

¹ Sterrenkundig Observatorium, Universiteit Gent, Krijgslaan 281 S9, 9000 Gent, Belgium
e-mail: marco.martorano@ugent.be

² Department of Astronomy, University of Michigan, 1085 South University Avenue, Ann Arbor, MI 48109–1107, USA

³ Cosmic Dawn Center (DAWN), Niels Bohr Institute, University of Copenhagen, Jagtvej 128, København N, DK-2200, Denmark

⁴ STAR Institute, Université de Liège, Quartier Agora, Allée du six Aout 19c, B-4000 Liege, Belgium

⁵ Department of Astronomy, University of Massachusetts, Amherst, MA 01003, USA

⁶ Department of Physics, University of Bath, Claverton Down, Bath BA2 7AY, UK

Received 16 June, 2025; accepted 28 November, 2025

ABSTRACT

Aims. We present the redshift evolution of radial color gradients (in rest-frame $U - V$ and $V - J$) for galaxies in the range $0.5 < z < 2.5$ and investigate their origin and dependence on stellar mass.

Methods. We select $\sim 10,200$ galaxies with stellar masses $M_\star > 10^{9.5} M_\odot$ from publicly available JWST/NIRCam-selected catalogs. Using 2D Sérsic profile fits to account for PSF broadening, we perform spatially resolved SED fitting on HST and JWST/NIRCam photometry retrieving accurate rest-frame $U - V$ and $V - J$ color gradients within $2R_{e, F444W}$.

Results. Star-forming galaxies generally exhibit negative $V - J$ color gradients that are strongly mass and redshift dependent. For massive star-forming galaxies ($M_\star > 10^{10.5} M_\odot$) at $z > 1.5$ $V - J$ colors are ≈ 0.5 mag redder within the effective radius than outside, on average. We find that, at all redshifts and across the entire stellar mass range, $V - J$ gradients strongly correlate with global attenuation (A_V), suggesting that they predominantly trace dust attenuation gradients. Edge-on galaxies are redder and have stronger gradients at all z , although the correlation weakens at higher z . The $U - V$ and $V - J$ color gradients in the quiescent galaxy population, in contrast, are weakly negative (from ≈ -0.1 to ≈ -0.2 mag), though significant, and show little or no dependence on stellar mass, redshift or axis ratio. The implication is that quiescent galaxies must be largely transparent, with low A_V , and color gradients mostly attributable to stellar population gradients.

Key words. galaxies: general – galaxies: evolution – galaxies: structure – galaxies: photometry – submillimeter: galaxies

1. Introduction

Galaxies in the local universe show red centers and bluer outskirts (i.e., Lin et al. 2017; Ellison et al. 2018) a characteristic attributed to gradients in the age and composition of stellar populations at different radii, as well as attenuation by dust. These color gradients have been deeply investigated since the early seventies (Sandage 1972) and their characteristics have been studied by many over the years (Peletier et al. 1990; de Jong 1996; Guo et al. 2011; Szomoru et al. 2013; Wuyts et al. 2013; Liu et al. 2016, 2017; Suess et al. 2019a; Miller et al. 2023; van der Wel et al. 2024). The color gradient in nearby quiescent galaxies can primarily be attributed to a radial metallicity gradient (i.e., Wu et al. 2005; Tortora et al. 2010, 2011; Sánchez-Blázquez et al. 2014; Goddard et al. 2017; Lin et al. 2024) with the additional possibility of an age gradient (La Barbera & de Carvalho 2009).

Color gradients in present-day star-forming galaxies arise from various factors (Bell & de Jong 2000). The inner parts have older and more metal-rich stellar populations (Bell & de Jong 2000; Zibetti & Gallazzi 2022), have lower star-formation activity (Tacchella et al. 2016; Lin et al. 2017; Belfiore et al. 2017, 2018; Ellison et al. 2018; Lin et al. 2019), and higher levels of attenuation (Greener et al. 2020). These factors are all physically correlated, but it is important to keep in mind that the ori-

gin of color gradients can vary from galaxy to galaxy: whereas the bulge of M31 has no ongoing star formation, other nearby spirals such as M51 and M101 have significant star formation throughout.

These results prompted an investigation of how these gradients emerged by looking at galaxies at earlier times, at higher redshift. The *Hubble* Space Telescope (HST) led the way to unveiling the rest-frame optical colors of galaxies up to redshift $z \sim 1$ (see, e.g., Hinkley & Im 2001; Menanteau et al. 2001; McGrath et al. 2008), showing color gradients were present also in those galaxies when the universe was ~ 6 Gyr old. The limited rest-frame optical wavelength range of these initial observations creates difficulties for disentangling dust and stellar population gradients: galaxies (or galaxy regions) can appear redder because of old/metal-rich stellar populations or due to increased dust attenuation. Near-IR emission at wavelengths between 1 and 3 μm , on the other hand, is less affected by dust attenuation and, therefore, allows us to separate between the effects of dust and stellar population gradients. Several authors (see e.g., Wuyts et al. 2012; Szomoru et al. 2013; Liu et al. 2016; Wang et al. 2017; Liu et al. 2017; Suess et al. 2020) have reported strong negative color gradients in high redshift galaxies, that is, their centers are redder than their outskirts. These gradients notably imply smaller half-light radii at longer wavelengths, and also more compact stellar

mass distributions than stellar light distributions (i.e., McGrath et al. 2008; Dutton et al. 2011; Guo et al. 2011; Wuyts et al. 2012; Szomoru et al. 2013; Mosleh et al. 2017, 2020; Suess et al. 2019b,a, 2020; Miller et al. 2023; van der Wel et al. 2024). However, the impact of dust on these trends has been difficult to confirm without a near-IR view, which is not obtainable with HST above redshift $z > 0.4$.

The *James Webb* Space Telescope NIRCam instrument solved this issue: its high angular resolution at near-IR wavelengths, comparable to that of HST in the optical, now allows us to investigate the rest-frame $> 1 \mu\text{m}$ wavelength range for galaxies up to redshift ~ 2.5 , when the universe was just ≈ 2.5 Gyr old. Early JWST results on a small sample of galaxies (54 star-forming galaxies with $M_\star > 10^{10} M_\odot$ and $1.7 < z < 2.3$) showed that galaxies exhibit strong negative color gradients up to $z = 2.3$ (Miller et al. 2022). These early findings are supported by several other works (e.g., Suess et al. 2022; Cutler et al. 2024; Ito et al. 2024; Ormerod et al. 2024; Martorano et al. 2024; Clausen et al. 2025) that measured sizes of high- z galaxies as a function of wavelength, and find that galaxies are systematically smaller in the near-IR than in the optical, consistent with the trends seen in the present-day universe. The early indications are that, at $z \approx 2$, dust gradients are more prominent than stellar population gradients, consistent with the notion of dust-obscured bulge growth at earlier cosmic times (Tadaki et al. 2017; Tacchella et al. 2018; Nelson et al. 2019; Tadaki et al. 2020). In fact, at high redshift, the highest A_V values are seen among the most massive galaxies (Price et al. 2014; Cullen et al. 2018; Lorenz et al. 2024; Nersesian et al. 2025; van der Wel et al. 2025), which have shallower optical profiles than in the near-IR (Martorano et al. 2025), suggesting that central mass concentrations – bulges or forming bulges – are present but strongly attenuated (see also Benton et al. 2024).

Using the complementarity of HST and JWST observations, we extend the early JWST results to a significantly larger sample of galaxies ($> 10,000$) with redshifts between 0.5 and 2.5 to investigate the origin and evolution across cosmic time of $U - V$ and $V - J$ color gradients. The two main goals are: (1) to determine the color gradients as a function of mass and galaxy type (star-forming vs. quiescent), and (2) to interpret the cause of the gradients and its evolution with cosmic time. The paper is structured as follows: in Section 2 we present an overview of the sample selection (Sect. 2.1), how we construct light profiles across wavelength (Sect. 2.2), how we measure resolved rest-frame $U - V$ and $V - J$ colors and give an overview of the global galaxy properties (Sect. 2.3); in Section 3 we present the results of this work: the color gradients (Sect. 3.1), their effect on the UVJ diagram (Sect. 3.2) and their relation with inclination as traced by the projected axis ratio (Sect. 3.3). Finally, in Section 4, we summarize our results and draw our conclusions. Throughout the paper we assume a standard Flat- Λ CDM cosmology with $H_0 = 70 \text{ km s}^{-1} \text{ Mpc}^{-1}$, $\Omega_m = 0.3$ and we adopt the AB magnitude system (Oke & Gunn 1983).

2. Data

2.1. Initial sample selection

The parent sample is drawn from the Dawn JWST Archive (DJA) morphological catalog¹. This catalog contains photometric and morphological measurements for over 400,000 galaxies in the

five CANDELS (Grogin et al. 2011; Koekemoer et al. 2011) fields observed with JWST/NIRCam over a plethora of different observational programs: e.g. PRIMER (Dunlop et al. 2021), COSMOS-Web (Casey et al. 2023), JADES (Eisenstein et al. 2023), FRESCO (Oesch et al. 2023), PANORAMIC (Williams et al. 2025), JEMS (Williams et al. 2023), and CEERS (Finkelstein et al. 2017, 2023).

Redshifts and global physical parameters (M_\star , rest-frame colors, A_V , which are relevant for this paper) are taken from the DJA morphological catalog as is. These were estimated via SED fitting running the code EAZY (Brammer et al. 2008) on $0.5''$ aperture photometry for all the available HST/ACS, HST/WFC3, JWST/NIRCam, and JWST/MIRI filters corrected to total fluxes. The high angular resolution and sensitivity of the four instruments on this wide wavelength range (from $0.4 \mu\text{m}$ to $21 \mu\text{m}$ though just for \approx half targets JWST/MIRI photometry is available) make it possible to recover accurate redshift measurements as well as stellar-mass measurements. EAZY was run on the *agn_blue_sfhz_13*² template set, which consists of 13 templates from the Flexible Stellar Populations Synthesis code (FSPS Conroy et al. 2009; Conroy & Gunn 2010) built with a Chabrier (2003) initial mass function (IMF) and a Kriek & Conroy (2013) dust attenuation law, a template derived from the NIRSspec spectrum of a $z = 8.5$ galaxy presented by Carnall et al. (2023) and a template generated to replicate the JWST/NIRSspec spectrum of a $z = 4.5$ source perhaps consistent with an obscured AGN torus (Killi et al. 2024). For all the details about the EAZY setup and the global photometry, we redirect the reader to Valentino et al. (2023).

From the parent sample, we select galaxies with an EAZY stellar mass $M_\star \geq 10^{9.5} M_\odot$. The low-mass, high-redshift galaxies selected via this mass threshold are at least 2 magnitudes brighter than the detection limit of the catalog in each field, implying that our sample is complete in stellar mass across the redshift range investigated here ($0.5 < z < 2.5$). An overview of the filters used throughout this work is presented in Table 1. We do not use JWST/MIRI imaging data because of the lower spatial resolution compared to HST and JWST/NIRCam. This limits our analysis up to rest-frame $\sim 1.3 \mu\text{m}$ at $z = 2.5$ and up to $\sim 3 \mu\text{m}$ at $z = 0.5$. The mosaics of the COSMOS and UDS fields are split in half with an overlapping region leading to some duplicate objects in the catalog. For these objects we only retain the one furthest from the mosaic's edges.

Our starting catalog includes 14,780 galaxies. Figure 1 shows nine representative galaxies divided into three stellar-mass bins at three (increasingly higher) redshifts. For each galaxy, we present three cutouts in the filters closer to the rest-frame U , V , and J bands, alongside their combination into an RGB image following a Richardson-Lucy deconvolution.

In Figure 2 we present an overview of the properties of the star-forming galaxies in our sample, showing the evolution of A_V with redshift in four stellar mass bins. We classify galaxies as star-forming or quiescent as in Muzzin et al. (2013) based on UVJ colors. For star-forming galaxies with $M_\star < 10^{10.5} M_\odot$, A_V shows little redshift dependence, specifically, A_V is ≈ 0.6 for $M_\star < 10^{10} M_\odot$ and ≈ 1.2 for $10^{10} < M_\star/M_\odot < 10^{10.5}$. More massive galaxies show a clear redshift evolution: from median $A_V \sim 1$ at $z \sim 0.5$ up to $A_V \sim 3$ at $z \sim 2.5$. For a more detailed examination of the evolution of the colors and dust attenuation, we refer to van der Wel et al. (2025).

¹ <https://dawn-cph.github.io/dja/blog/2024/08/16/morphological-data/>

² <https://github.com/gbrammer/eaazy-photoz/tree/master/templates/sfhz>

Table 1. Filters used throughout the work for Sérsic profile fitting and to compute rest-frame colors.

COSMOS	HST/ACS HST/WFC3 JWST/NIRCam-SW JWST/NIRCam-LW	F435W F606W F814W F125W F140W F160W F090W F115W F150W F200W F277W F356W F410M F444W
UDS	HST/ACS HST/WFC3 JWST/NIRCam-SW JWST/NIRCam-LW	F435W F606W F814W F125W F140W F160W F090W F115W F150W F200W F277W F356W F410M F444W
GOODS-S	HST/ACS HST/WFC3 JWST/NIRCam-SW JWST/NIRCam-LW	F435W F606W F775W F814W F105W F125W F140W F160W F090W F115W F150W F182M F200W F210M F277W F335M F356W F410M F444W
GOODS-N	HST/ACS HST/WFC3 JWST/NIRCam-SW JWST/NIRCam-LW	F435W F606W F775W F814W F105W F125W F140W F160W F090W F115W F150W F182M F200W F210M F277W F335M F356W F410M F444W

The existence of a population of dusty galaxies at $z \gtrsim 2$ has, of course, been known for decades, both from near-IR surveys (Franx et al. 2003; Daddi et al. 2004; Labbé et al. 2005; Wuyts et al. 2007), far infrared surveys (e.g., Shirley et al. 2019), and surveys at mm wavelengths (e.g., Smail et al. 1997, 2002; Chapman et al. 2003; Daddi et al. 2007). To provide this context, we cross-match our catalog with the A^3 COSMOS and A^3 GOODSS catalogs (Adscheid et al. 2024) that contain all galaxies identified by ALMA during all the programs that surveyed the COSMOS and GOODS-S fields. We find a match for 92 sub-mm galaxies with a separation below $0.4''$ (these are indicated by diamond markers throughout the work). These sub-mm galaxies are mostly seen at $z > 1.5$ and tend to be more massive than $M_\star > 10^{10.5} M_\odot$. All are characterized by the reddest $V - J$ colors and have a median $A_V \sim 3$. According to their UVJ colors and to the definition of quiescence adopted throughout this work (Muzzin et al. 2013), all these 92 galaxies are classified as star-forming. This sub-mm detected sample is not complete or representative for our sample; it is included to highlight the link between highly attenuated galaxies and dust emission-selected samples, as also done in van der Wel et al. (2025).

2.2. Sérsic Profile Fits

To quantify color gradients, we use multi-wavelength Sérsic profile fits. While these are crude, summary descriptions of the light distribution, they address two important problems. First, the profile fits account for the wavelength-dependent PSF effects, which flatten color gradients as seen directly in the images (see e.g., Fig. 1). Second, pixel-to-pixel variance is averaged out. To fairly compare color gradients between galaxies with a large variety of sizes and redshifts, we measure colors and gradients in apertures relative to the half-light radius using photometry based on the galaxies' 2D brightness model approximated with a single Sérsic profile. We thus perform Sérsic profile fitting of all the galaxies using the code GALFITM (Häußler et al. 2013; Vika et al. 2013), a further developed version of GALFIT (Peng et al. 2002, 2010). The setup is overall the same as presented in Martorano et al. (2024) with minor differences.

Briefly, for each field we create a segmentation map using the code SEP (Bertin & Arnouts 1996; Barbary 2016) using as detection image a stack of all long-wavelength JWST/NIRCam filters available (see Table 1 for the complete list of filters). We

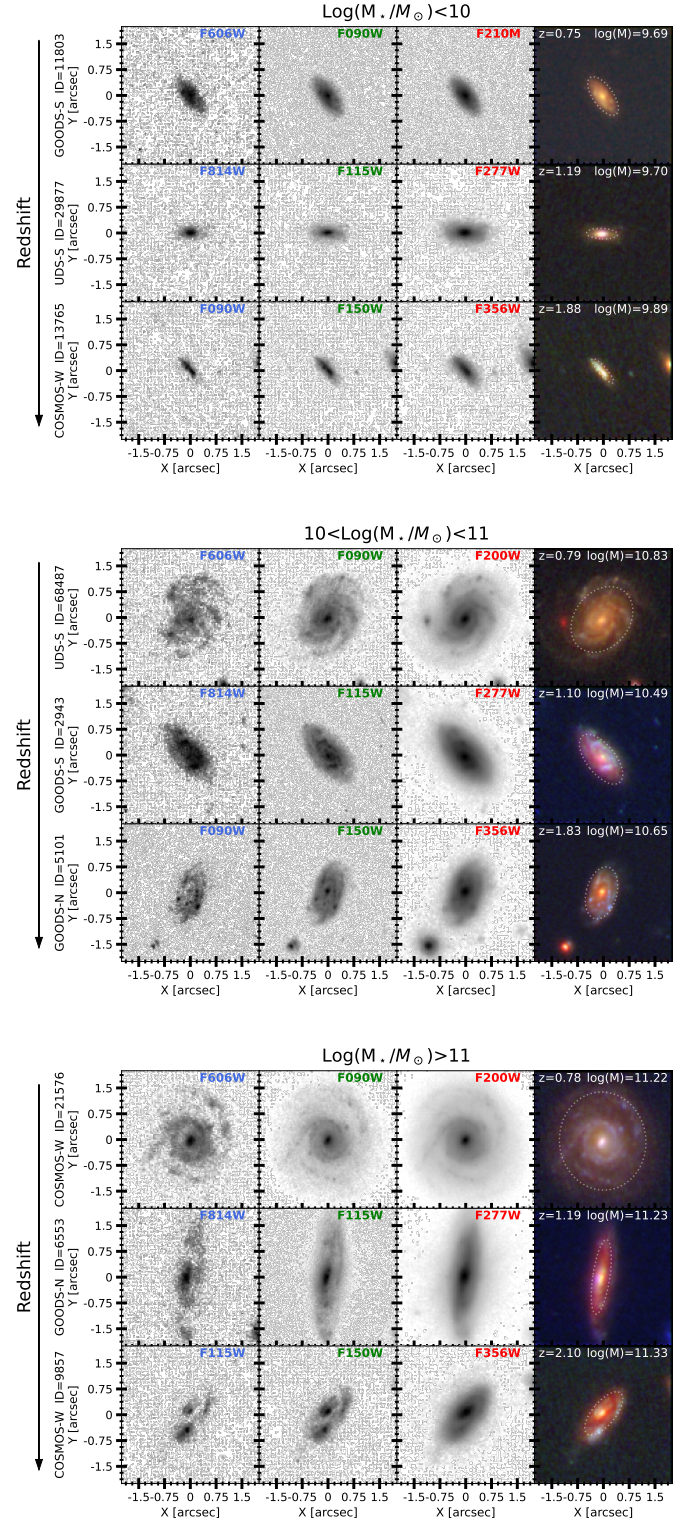


Fig. 1. Example of 9 galaxies used in the work (field and DJA ID shown on the left of each row) divided into 3 sets according to their stellar mass and ordered by redshift. For each galaxy, we present cutouts in the three filters that closely match the rest-frame U(blue)-V(green)-J(red) bands. While the grey panels show the original images, to create the RGB images each filter was first deconvolved with a Richardson-Lucy algorithm. On the RGB image we overplot ellipses with semi-major axis twice the effective radii measured in JWST/NIRCam F444W as described in Sect. 2.2.

set a detection threshold at 3σ , a minimum area of 5 pixels and

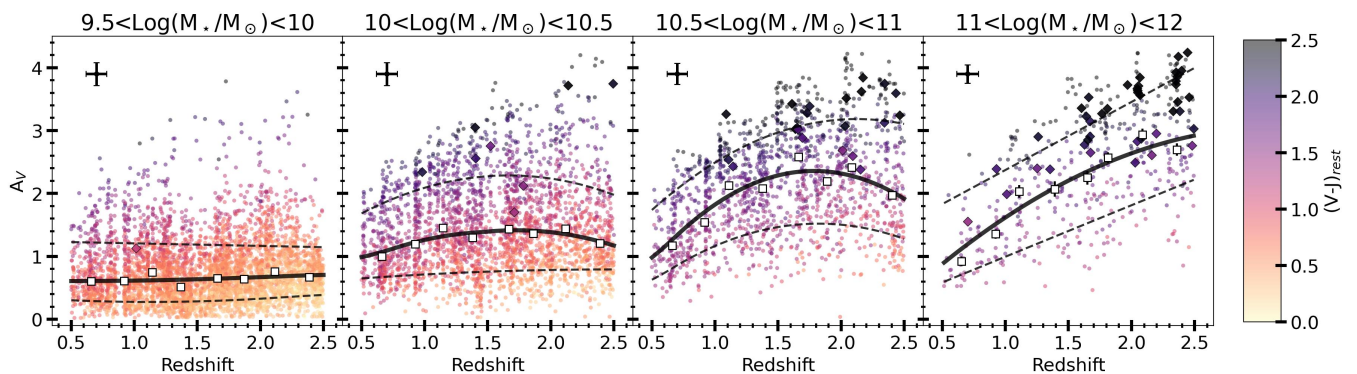


Fig. 2. Attenuation in the V -band (A_V) as a function of redshift in four stellar mass bins for star-forming galaxies color-coded with their $V - J$ color. White squares show the median in stellar mass bins and error bars the statistical uncertainty (σ/\sqrt{N}). The solid black lines show the spline-percentile regression while the dashed lines show the 16-84 percentiles of the distribution. Diamonds highlight sub-mm selected galaxies. In the top left corner of each panel we show the median (16-84)/2 percentile ranges of the posterior distributions of A_V and redshift as provided by EAZY. Massive galaxies at high redshift are redder and more attenuated than their lower redshift counterparts.

a contrast ratio for object deblending of 0.02. For each source in the parent sample, we create cutouts large enough to contain 25 times more pixels available for background estimation than pixels falling in a segment. We set a minimum size of the cutout of $8''$ and a maximum of $20''$. Following Martorano et al. (2023) we fit simultaneously with the main source all objects identified in the segmentation map that are brighter (or up to one magnitude fainter) than the target. This ensures that the light of bright objects in the cutouts is properly subtracted, hence allowing for a better estimate of the background. Any other source in the cutout is masked with the corresponding segment of the segmentation map. The background is left as a free parameter in the fit performed by GALFITM. For each galaxy, we provide GALFITM with initial estimates for the position, magnitude, effective radius, and axis ratio based on the results obtained from the SEP analysis, while the initial guess for the position angle is set to 0 and for the Sérsic index to 2.3.

For each filter we retrieve a Point Spread Function (PSF) using the same procedure outlined in Martorano et al. (2024): we select a sample of candidate stars from the size-brightness relation in the filter F444W, and observed in all the available filters; we masked all sources within $3''$ and rejected those candidate stars with nearby bright objects which could potentially bias the background. From this set of objects, we visually select the most suitable stellar candidates: isolated, bright, but not saturated in the center. The selected stars are stacked after normalizing their $0.3''$ aperture flux and background subtraction. For JWST/NIRCam, we match the flux of the stacked PSF in an annulus between $2.5''$ and $3''$ to the flux in the same annulus of the model PSF computed with WEBBPSF (Perrin et al. 2014). This guarantees that any low-level residual background in the stacked PSF is removed. The PSFs obtained are used as input for GALFITM.

Throughout this work, we assume as reference filter F444W. We discard all galaxies whose fit in this filter failed or did not reach convergence for one of the parameters ($\sim 4\%$ of the whole sample). M.M. visually inspected the fit results for all the galaxies, flagging and removing evident mergers, gravitational lenses, and those where the flux of bright sources near the target strongly pollutes the photometry of the target itself. In addition, objects defined as segments including multiple bright peaks are removed. Finally, 22 galaxies are removed whose Sérsic index value in F444W hit the fit boundaries of 0.2-10. In total, another 5% of the sample are thus rejected, leaving 13,332 galaxies for

which useful color gradients can be measured. The rejected targets are evenly distributed in stellar mass and redshift hence their removal does not severely bias our sample.

For each galaxy, we compute rest-frame $0.5\ \mu\text{m}$ and $1.5\ \mu\text{m}$ effective radii ($R_{e,0.5\ \mu\text{m}}$ and $R_{e,1.5\ \mu\text{m}}$, respectively) fitting a second-order Chebyshev polynomial to all the effective radii calculated in the filters investigated as a function of wavelength. We iterate this procedure 1000 times Gaussian sampling the R_e measurements from their uncertainty distributions. We consider the best polynomial the one made of the median of the coefficients retrieved. The same procedure is repeated to compute the Sérsic index at rest-frame $0.5\ \mu\text{m}$ ($n_{0.5\ \mu\text{m}}$) and $1.5\ \mu\text{m}$ ($n_{1.5\ \mu\text{m}}$).

2.3. $U - V$ and $V - J$ Rest-Frame Color Gradients

Using the parameters recovered from the Sérsic profile fitting presented in Section 2.2, we construct images of the intrinsic Sérsic profile (not PSF-convolved) in each filter. We measure fluxes within an ellipse whose center, semi-major axis, position angle, and axis ratio are taken from the F444W Sérsic profile fit. Likewise, we measure aperture photometry in an elliptical annulus between 1 and $2 R_{e,F444W}$.³ We do not add flux residuals as done by, e.g., Szomoru et al. (2010) and Suess et al. (2019a) to account for imperfections in the single Sérsic profile fits. The benefits of this approach do not, for our purposes, outweigh the additional uncertainties (noise). To verify that this is the case, we measure the residual F150W–F115W and F356W–F150W colors in the two apertures and their effect on the measured color gradient from the Sérsic profiles. These filters cover rest-frame U , V , and J at $z \approx 2$. The average change in the colors (and gradients) is $< 1\%$ and the scatter just 3%, which implies that the simplified description of the light profiles with single Sérsic profiles does not lead to relevant systematic effects in the measured color gradients (see Appendix A).

We use EAZY to derive rest-frame U , V and J fluxes by fitting the SED of both apertures, fixing the redshift at the value from the DJA catalog, and also adopting the same setup and zero-points as those used for the DJA catalog ensuring this does not induce systematic biases when comparing rest-frame fluxes retrieved in this work with those in the parent catalog. We de-

³ $R_{e,F444W}$ traces different rest-frame wavelengths at different redshift. Using the rest frame aperture $R_{e,1.5\ \mu\text{m}}$ does not change the results presented in this work.

fine the color gradient as the color difference between the outer ($1 - 2 R_{e,F444W}$) and inner ($< R_{e,F444W}$) apertures, adopting the convention that a galaxy with a red center and blue outskirts has a negative color gradient.

The use of deconvolved Sérsic profile models for the aperture photometry corrects for PSF effects that flatten gradients in the original, PSF-convolved images, especially for small galaxies. The drawback of this method is the reliance on the single-component Sérsic models and the quality of the fits.

To avoid the effects of template mismatch, we require that for each of the rest-frame U , V , J bands at least 50% overlaps with at least one of the HST or JWST filters listed in Table 1. That way, the calculated rest-frame colors minimize interpolation by approximating the rest-frame colors to observed ones, without strong template dependencies. $\approx 22\%$ of the galaxies are rejected by this constraint. Rejected galaxies are roughly uniformly distributed in redshift due to the field-to-field variation in filter sets, with the clear exception of lacking rest-frame J -band coverage at $0.88 < z < 0.90$ due to the large gap between F200W and F277W. We note that the rejected 22% do not strongly affect the median trends in the results below, but they would have caused an increase in scatter due to the larger uncertainties induced by the interpolation between filters by EAZY.

The final sample contains 10,359 galaxies, of which 9,444 are star-forming and 915 are quiescent. 71 out of the original 92 sub-mm selected galaxies survived the selection.

3. Results

The superb angular resolution of JWST in the rest-frame near-IR and extensive wavelength coverage provided by the synergy of HST and JWST allows us to probe beyond the global colors of galaxies, bringing into view the color gradients within them. Figure 1 already demonstrates a visually striking presence of color gradients in a small sample of galaxies. The galaxies in the figure are representative of three stellar mass bins and three redshift bins. While low-mass galaxies show similar colors and mild color gradients at any redshift, for $M_\star > 10^{10.5} M_\odot$, galaxies at $z > 2$ are systematically redder than at $z < 1$, and also have cores that are redder than the outskirts. For the same set of 9 galaxies shown in Figure 1, in Figure 3 we present the $U - V$ and $V - J$ color gradients showing the variation of the colors up to $2 R_{e,F444W}$ on the UVJ plane. We also plot a grid of expected UVJ colors as a function of stellar metallicity and ages using the BPASS stellar libraries v.2.3.1 with solar $[\alpha/Fe]$ (Byrne et al. 2022) together with the A_V vector that represents the impact of a simple dust screen as modelled within the THEMIS modeling framework (Jones et al. 2017). The low-mass galaxies show just mild color gradients at any redshift while for higher stellar masses, color gradients are systematically stronger, with $U - V$ and $V - J$ changing by up to 1 mag between the core and the outskirts of the galaxy. The colors and color gradients for low mass galaxies seem compatible with a combination of age and metallicity gradients, while, at higher stellar masses, the need of dust (possibly with non-standard geometries) to redden the templates is clear. To support the qualitative color gradient trends shown in this Figure, in the next sections we quantify how the color gradients vary with global galaxy properties and redshift.

3.1. Color gradients

In Figures 4 and 5 we present the $U - V$ and $V - J$ color gradients (hereafter $\Delta(U - V)$ and $\Delta(V - J)$ respectively) of star-forming

and quiescent galaxies as a function of redshift and in four different stellar mass bins. In the lower part of each panel, we show the median uncertainty on the color gradients (Appendix B). The solid black lines show the running median computed with the COBS library (Ng & Maechler 2007, 2022), which allows for a smoothed combination of a spline regression and quantile regression, highlighting non-linear trends.

Figure 4 shows that, on average, quiescent galaxies display mild $U - V$ gradients, with $\Delta(U - V) \approx -0.1$ mag, independent of redshift and mass. Their median $\Delta(V - J)$, in contrast, shows a mild redshift dependence: galaxies at $z > 2$ and $M_\star < 10^{10.5} M_\odot$ show stronger gradients than their lower redshift counterpart, whereas this redshift evolution weakens and disappears at higher stellar mass (Spearman coefficients: for $M_\star < 10^{10.5} M_\odot$ $\rho = -0.26$ while for $M_\star > 10^{10.5} M_\odot$ $\rho = -0.06$). As highlighted by the dashed lines showing the 16-84 percentiles, for low mass galaxies the scatter in the color gradients strongly increases with redshift. This increased scatter is mostly due to the larger uncertainties in the color gradients (as shown by the systematically larger error bars in the bottom right corner), and suffers from small number statistics. We visually inspected galaxies with gradients stronger than the 16th percentile (outliers) and found that, in most cases, the gradients are highly uncertain, with a small subset of objects with genuinely strong gradients. Conversely, for massive quiescent galaxies, the uncertainty in the color gradients exhibits only mild redshift dependence, reflecting the relative ease of measurement in larger objects (see, e.g., Martorano et al. 2024) and the absence of pronounced galaxy-to-galaxy variations. The low number of low-mass quiescent galaxies at high redshift, combined with the larger uncertainties in their color gradients, reduces our confidence in claiming a physical trend with redshift for these objects despite the values retrieved for the Spearman coefficient. The global A_V of quiescent galaxies also varies mildly with redshift, increasing up to $A_V \approx 1$ (van der Wel et al. 2025) as can be expected from their higher sSFR at high- z (e.g., Leja et al. 2022). However, the A_V estimates of such systems might be questionable given the systematic uncertainties related to our limited knowledge of the intrinsic near-IR colors of evolved stellar populations. Nevertheless, color gradients in quiescent galaxies primarily appear to originate with gradients in their stellar population (as also suggested by the BPASS comparison in Figure 3) rather than by strong dust gradients (see also e.g., Suess et al. 2020).

The conclusions change for star-forming galaxies (Fig. 5). These are characterized by generally negative $\Delta(U - V)$, except at the low-mass end ($M_\star < 10^{10} M_\odot$), where star-forming galaxies show no $U - V$ gradients at $z > 1.5$, with the scatter dominated (as for quiescent galaxies) by random uncertainties due to limited sensitivity in the rest-frame U band. Higher-mass galaxies have slightly stronger $\Delta(U - V)$, though with no or only weak redshift dependence. We find that $\Delta(U - V)$ is uncorrelated with global A_V (Spearman rank correlation coefficient ≈ 0.1). The $\Delta(U - V)$ gradients are broadly comparable with the HST-based $U - V$ gradients presented in Wuyts & Förster Schreiber (2020) despite the different methodology and photometry (they investigate color gradients measuring $\Delta(U - V)$ in apertures smaller and larger than 2 kpc).

The $V - J$ gradient $\Delta(V - J)$ shows more variation than $\Delta(U - V)$, as well as stronger and more interesting trends with stellar mass and redshift. The uncertainties are small, even at large z , thanks to the exquisite depth of the NIRC2 imaging. Gradients are significantly negative in general, even for low-mass galaxies (see also Miller et al. 2023, where $g - r$ gradients are investigated). There is a strong mass-dependence and

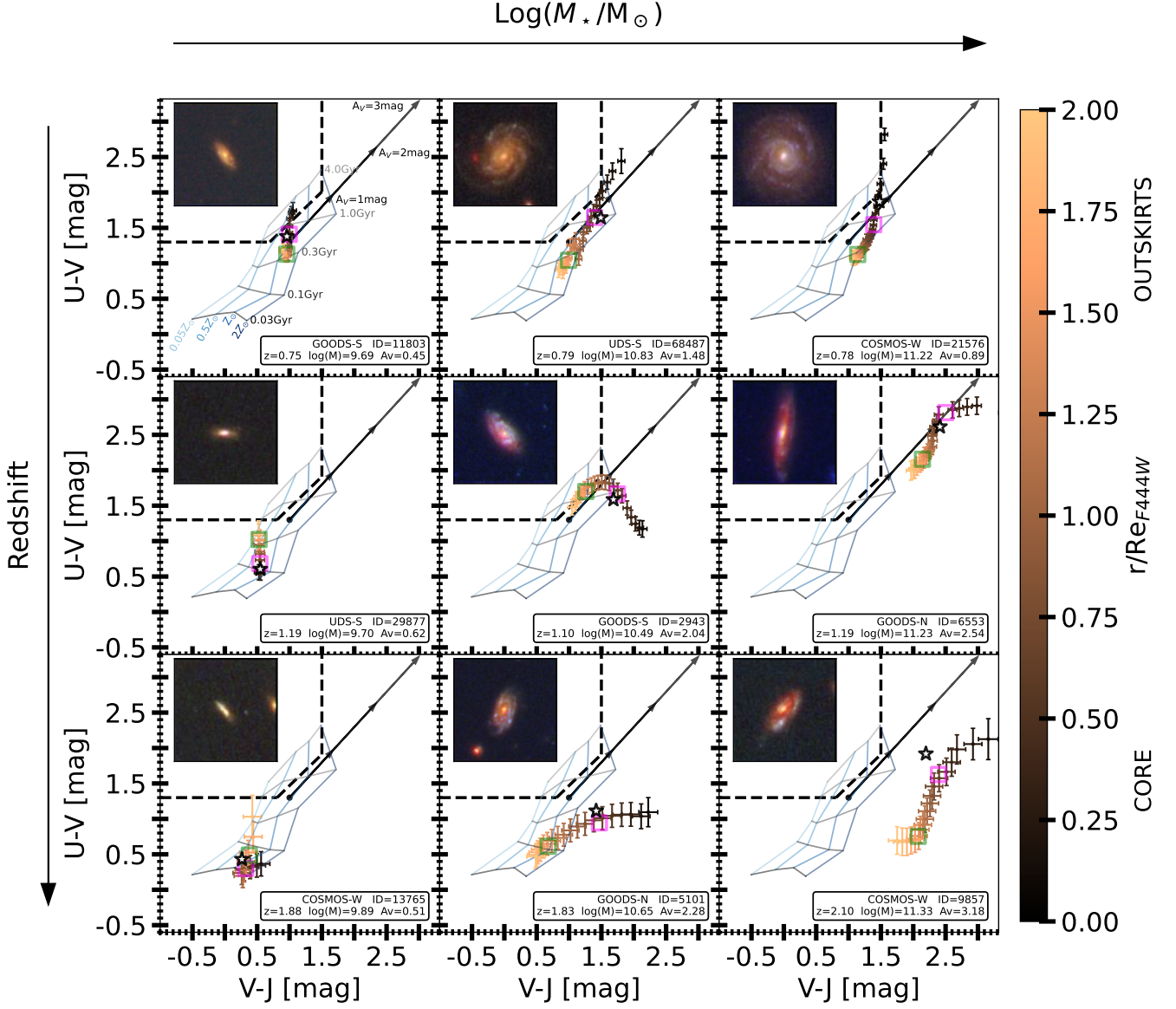


Fig. 3. UVJ plots for the same galaxies presented in Figure 1. Each panel shows the UVJ color gradients in elliptical apertures of width $0.04''$ up to an aperture twice the effective radius in the filter F444W. Dashed black lines identify the quiescent region as defined in Muzzin et al. (2013). The white star with black contour shows the UVJ colors of the galaxy as in the DJA catalog, while the magenta (green) squares show the color measured within R_e ($1 - 2R_e$). In the bottom right corner we report the field and ID of the galaxy, together with its redshift, stellar mass and global A_V . In each panel we show a grid of metallicities and ages from the BPASS stellar libraries together with the theoretical A_V vector induced by a dust screen. This figure showcases different kind of color gradients across galaxies in the sample.

a strong redshift dependence for higher-mass galaxies ($M_\star > 10^{10.5} M_\odot$): the median and scatter are very large at $z > 1.5$. $\Delta(V - J)$ correlates strongly with global A_V (Spearman rank correlation coefficient of ≈ -0.6). The emergence of large fractions of high- A_V galaxies at $z > 1.5$ discussed above goes hand in hand with the emergence of strong $V - J$ color gradients. Among galaxies with $A_V > 2$, gradients of $\Delta(V - J) \approx -1$ mag are not uncommon: these galaxies are 1 magnitude redder within their effective radius than outside. The large variation among massive star-forming galaxies at high redshift is not (entirely) due to uncertainties, but reflects a true galaxy-to-galaxy difference in dust properties and viewing angle. This is further addressed in Section 3.3. For reference, the population of 71 sub-mm selected galaxies in our sample have a median $A_V = 3.1^{+0.6}_{-0.7}$, and $\Delta(U - V) = -0.2^{+0.2}_{-0.3}$ mag and $\Delta(V - J) = -0.7^{+0.4}_{-0.3}$ mag, com-

parable to the general population of high- A_V star-forming galaxies, suggesting a link between IR-bright galaxies and centrally concentrated dust distributions.

Contrary to present-day massive galaxies, in which color gradients are driven by a combination of star-formation, age, and metallicity gradients (Tortora et al. 2010, 2011; La Barbera & de Carvalho 2009), our results imply that for $M_\star > 10^{10.5} M_\odot$ the main driver of the color gradients in $z > 1$ galaxies is attenuation by dust. Several authors using other colors (i.e., Liu et al. 2016, 2017; Nelson et al. 2016; Wang et al. 2017) or methodologies (Miller et al. 2022, 2023; van der Wel et al. 2024; Martorano et al. 2024) reached the same conclusion. Strong color gradients, together with a characteristically high A_V in massive star-forming galaxies at $z > 1$ imply that these galaxies are building (or have already built) a core through intensive attenuated star-formation that is unveiled when seen in the near-IR (Nelson

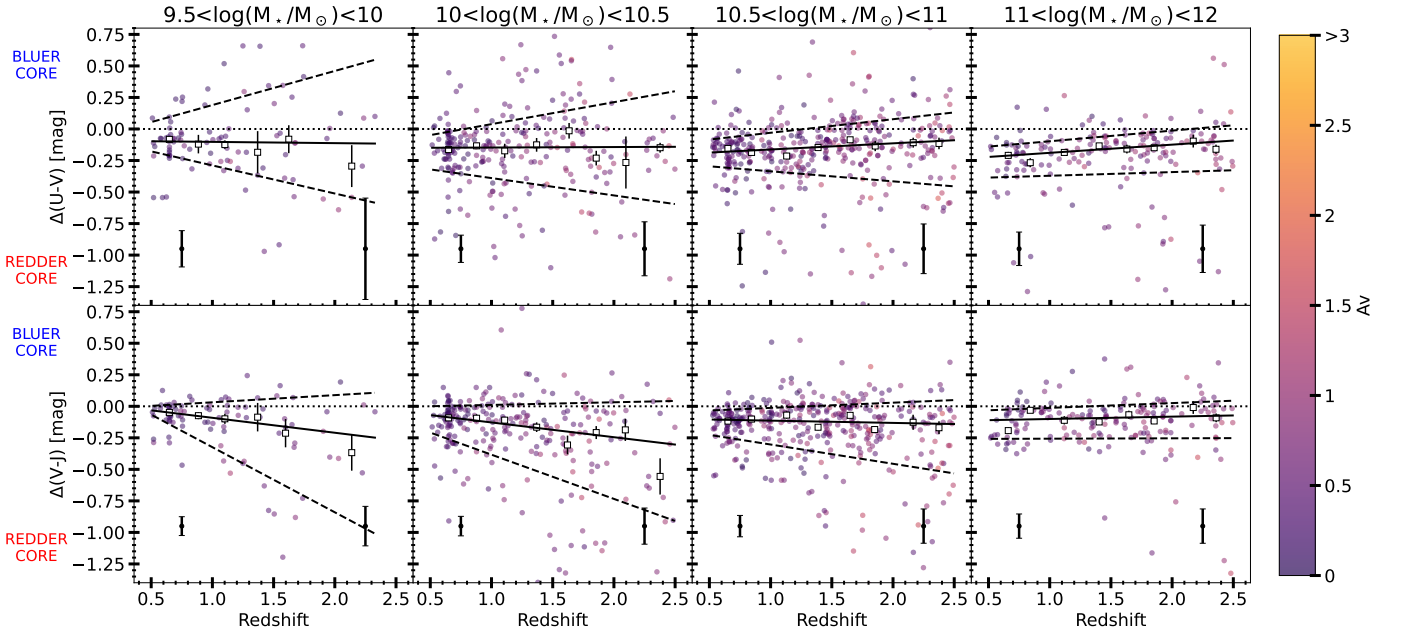


Fig. 4. Color gradients as a function of redshift for quiescent galaxies in four stellar mass bins and color-coded with global A_V . The top row shows the $U - V$ color gradients ($\Delta(U - V) = (U - V)_{1 < r/R_c < 2} - (U - V)_{r < R_c}$) while the bottom row shows the $V - J$ color gradients ($\Delta(V - J) = (V - J)_{1 < r/R_c < 2} - (V - J)_{r < R_c}$). Black error bars in the lower left (right) corner of each panel show the median uncertainty on color gradients for all the galaxies in that stellar mass bin with $z < 1.5$ ($z > 1.5$). Solid black lines show the running median; dashed lines show the 16-84 percentile range. Squares show the median color in redshift bins of width 0.25 with (generally negligible) error bars representing the statistical uncertainty σ/\sqrt{N} . Both colors show a mild stellar mass dependence and a mild or absent redshift evolution. Just galaxies with $M_* < 10^{10.5} M_\odot$ show a significant evolution of $\Delta(V - J)$ with redshift.

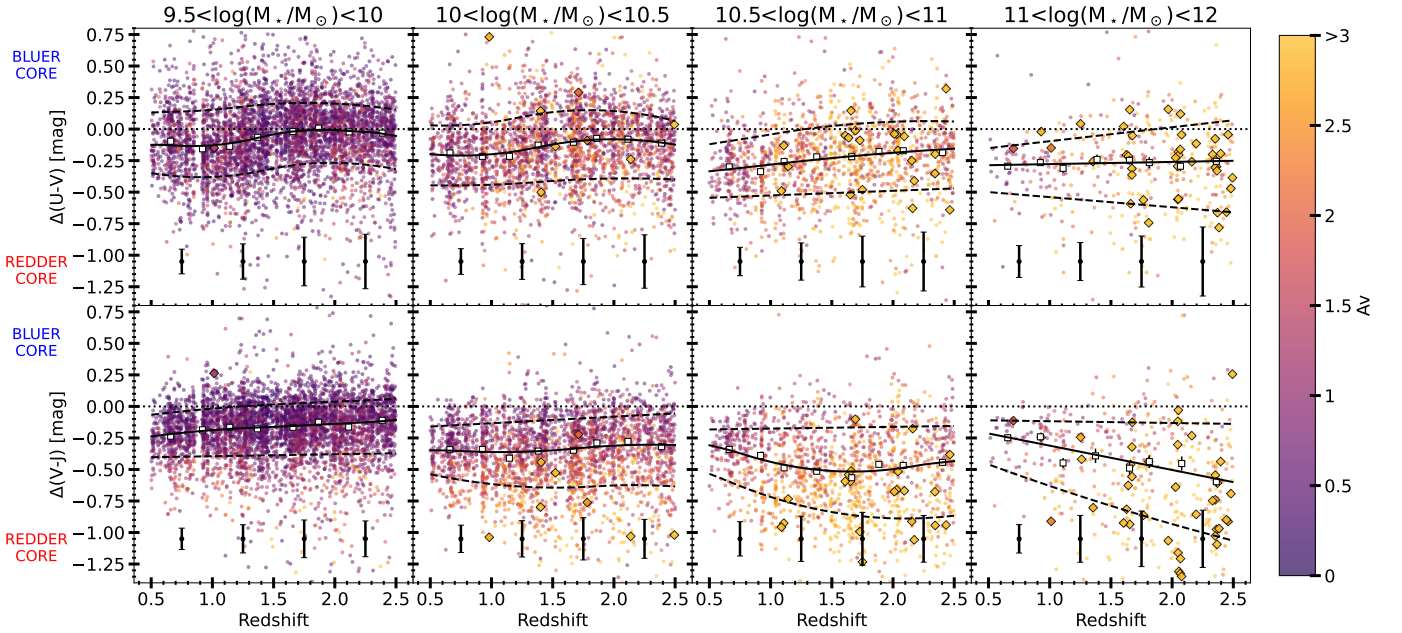


Fig. 5. Same as Fig. 4 but for star-forming galaxies. Diamonds identify sub-mm selected galaxies. Black error bars in the lower part of each panel show the median uncertainty on color gradients at that redshift. $\Delta(U - V)$ show no discernible redshift dependence and low-mass galaxies show no $U - V$ gradients at $z > 1.5$. Conversely, $\Delta(V - J)$ shows a strong mass and redshift dependence.

et al. 2016, 2019; Miller et al. 2022; Le Bail et al. 2024; Benton et al. 2024; Tan et al. 2024; Nedkova et al. 2024; Martorano et al. 2025; Maheson et al. 2025). Evidence for bulge building in heavily dust obscured galaxy cores at $z \sim 2$ has also been revealed using high-resolution ALMA $870 \mu\text{m}$ imaging (e.g., Hodge et al. 2016; Tadaki et al. 2017, 2020). In Appendix C we compare the color gradients computed in this paper with the corresponding

size ratio at different wavelengths. While these quantities both arise from changes in the light profile with wavelength, they are not identical.

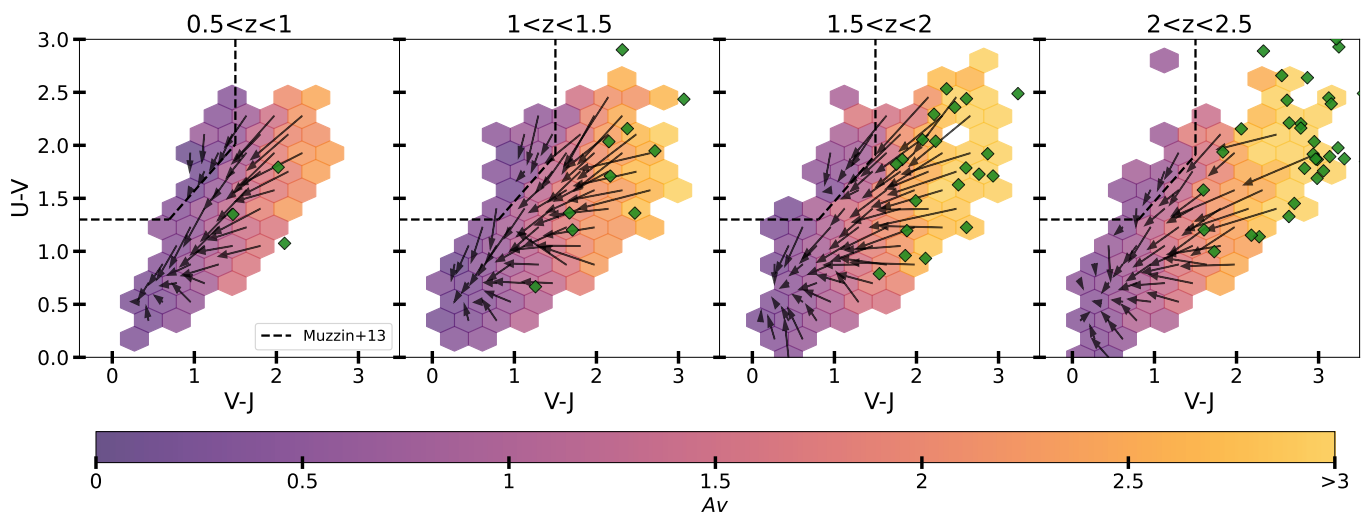


Fig. 6. UVJ diagram of colors measured within the F444W effective radius, with hexbins containing at least five galaxies color-coded with the median global A_V . The length and direction of the arrows indicate the median color shift from within the effective radius to the aperture between $1R_e$ and $2R_e$, following our definition of color gradient throughout this paper. A minimum of 10 galaxies in the hexbin was required for drawing an arrow. Green diamonds highlight the $U - V$ and $V - J$ colors within $1R_e$ for the sub-mm selected sample.

3.2. Color gradients in the UVJ diagram

The color gradients presented in section 3.1 have a major impact on the UVJ diagram, frequently used (as in this paper) to separate star-forming and quiescent galaxies. In Figure 6, we present the UVJ diagram using the rest-frame $U - V$ and $V - J$ colors within the effective radius, computed from elliptical aperture photometry with semi-major axis equal to $R_{e,F444W}$.

Similarly to global colors (see Figure 2 and van der Wel et al. 2025), the central colors, computed within $1R_e$, strongly correlate with the global A_V , with highly attenuated galaxies showing the reddest $U - V$ and $V - J$ colors. Once again, we see the emergence of a significant population of galaxies with very red centers ($V - J \approx 3$) at $z > 1$, but without a noticeable reddening in $U - V$. The color gradients, indicated by the black arrows in Figure 6, move the colors toward the bottom left corner of the UVJ plane, as expected for attenuation. Galaxies with the bluest central $U - V$ colors (bottom left corner of each panel) show positive $\Delta(U - V)$ and mild or absent $\Delta(V - J)$, suggesting they are undergoing a central starburst. Conversely, star-forming galaxies with $V - J < 1$ mag and $U - V > 0.6$ mag show $\Delta(U - V) < 0$ and $\Delta(V - J) \approx 0$, perhaps a sign of inside-out quenching (Tacchella et al. 2016) or of post-starburst systems (e.g., Belli et al. 2019).

As we already witnessed in Figures 4 and 5, quiescent galaxies are characterized by relatively mild color gradients. For $z < 1$ (leftmost panel of Fig. 6) there are as many galaxies with quiescent centers and star-forming outskirts as vice versa ($\approx 35\%$ of the quiescent population with $z < 1$), and their median gradients are very small, putting both centers and outskirts within or near the quiescent boundary. Conversely, for $z > 1$, there are ~ 3 times more galaxies with star-forming centers and quiescent outskirts than the other way around. Those with star-forming center have relatively weak $\Delta(U - V) = -0.1^{+0.3}_{-0.3}$ mag but strong $\Delta(V - J) = -0.4^{+0.3}_{-0.4}$ mag (e.g., almost horizontal arrows in Fig. 6). The colors are too red to be explained by metallicity gradients, but rather require a grey attenuation curve in the UV-optical, which is indeed seen for more attenuated galaxies (Salim et al. 2018; Barišić et al. 2020). The high A_V value of galaxies with near-horizontal gradient arrows in Fig. 6 suggest that dust gradients are the likely explanation of the color

gradients. Under this assumption, these galaxies have obscured, star-forming cores and quiescent, less attenuated outskirts. In the small subset of galaxies with quiescent cores and star-forming outskirts, the pattern is consistent with that observed in some present-day massive galaxies such as M31. These exhibit strong $\Delta(U - V) = -0.4^{+0.2}_{-0.5}$ mag but weak $\Delta(V - J) = 0.0^{+0.1}_{-0.2}$ mag (see e.g., Fig. 3 top left panel). This may imply a genuine population gradient (i.e., Ellison et al. 2018, and references therein) like M31, or at least a gradient in star-formation activity, which affects $U - V$ more than $V - J$ (e.g., Gebek et al. 2025). Truly quiescent cores such as in M31 are relatively rare. Instead, it is more common to have star formation throughout, such as in local spiral galaxies like M51, M83, M101 and the Milky Way. The color gradients are generally caused by a combination of factors, varying from galaxy to galaxy. Cosmological simulations are the ideal framework for properly identifying the factors responsible for global colors and color gradients. At present, however, these still have problems describing all the features in observed UVJ diagrams (Donnari et al. 2019; Akins et al. 2022; Gebek et al. 2025). Following Gebek et al., however, we might expect our results to imply a specialized dust geometry; those authors find that obtaining large $V - J$ colors without strongly affecting the distribution of $U - V$ colors requires birthcloud-like attenuation around all stars younger than 1 Gyr.

The sub-mm selected galaxies, which are among the most attenuated of all galaxies in our sample, lay almost all in the top right corner of the UVJ diagram and have similar color gradients to all other galaxies with $A_V > 3$. Only four out of the 71 sub-mm galaxies show color gradients resembling a star-forming core and quiescent outskirts. Two of them show extended disks with spiral arms and hints of ongoing minor mergers. The other two show no morphological features.

3.3. Color gradients and axis ratios: trends with inclination

The results presented in the previous sections indicate that, in massive star-forming galaxies at $z > 1.5$, dust attenuation in the rest-frame V -band is centrally concentrated within galaxies. At lower z , integrated (galaxy-averaged) A_V values are lower and gradients weaker. To further explore the nature of this evolu-

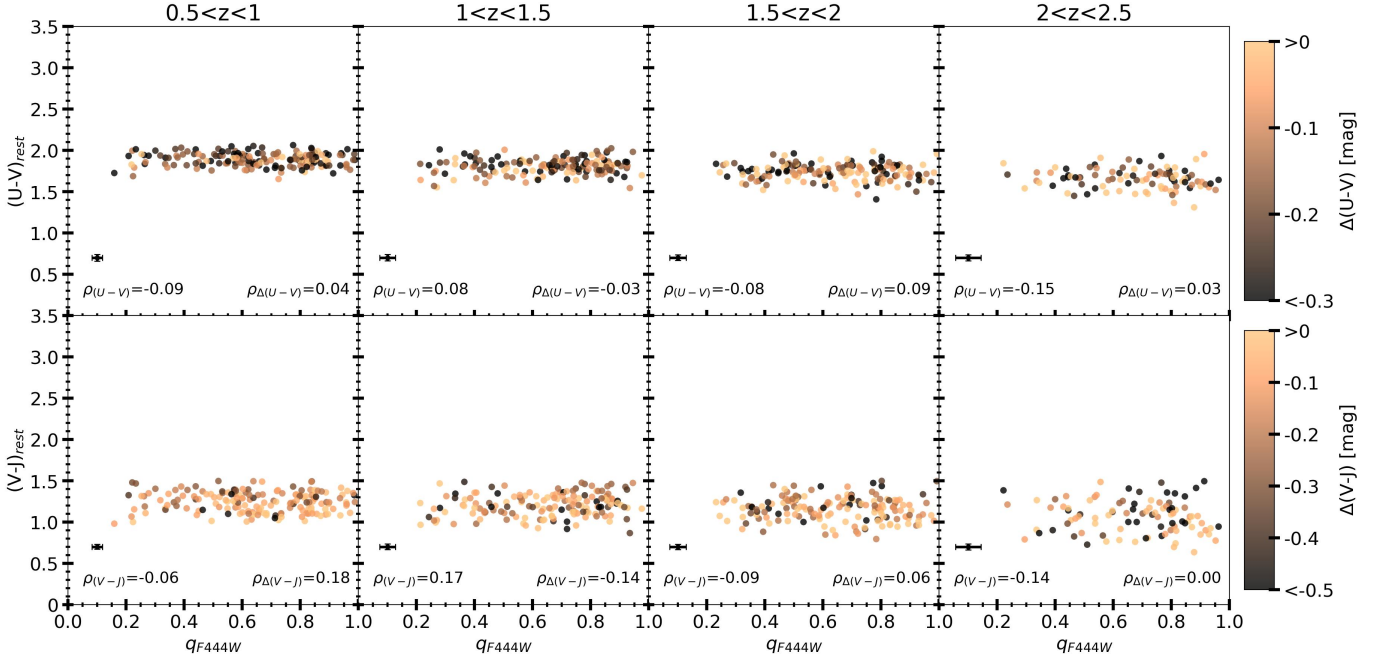


Fig. 7. Projected axis ratio (q) observed in JWST/NIRCam-F444W against $U - V$ (upper panels) and $V - J$ (lower panels) colors in four redshift bins. Color-coding shows the color gradient computed as the difference between the color between $1-2R_e$ and $0-1R_e$. Just quiescent galaxies with stellar mass $M_\star \geq 10^{10.5} M_\odot$ are shown. In the lower left corner, we show the median uncertainties on the rest frame colors and axis ratios and the Spearman correlation coefficient between the axis ratio and the color, while in the right corner, we show that between the axis ratio and the color gradient.

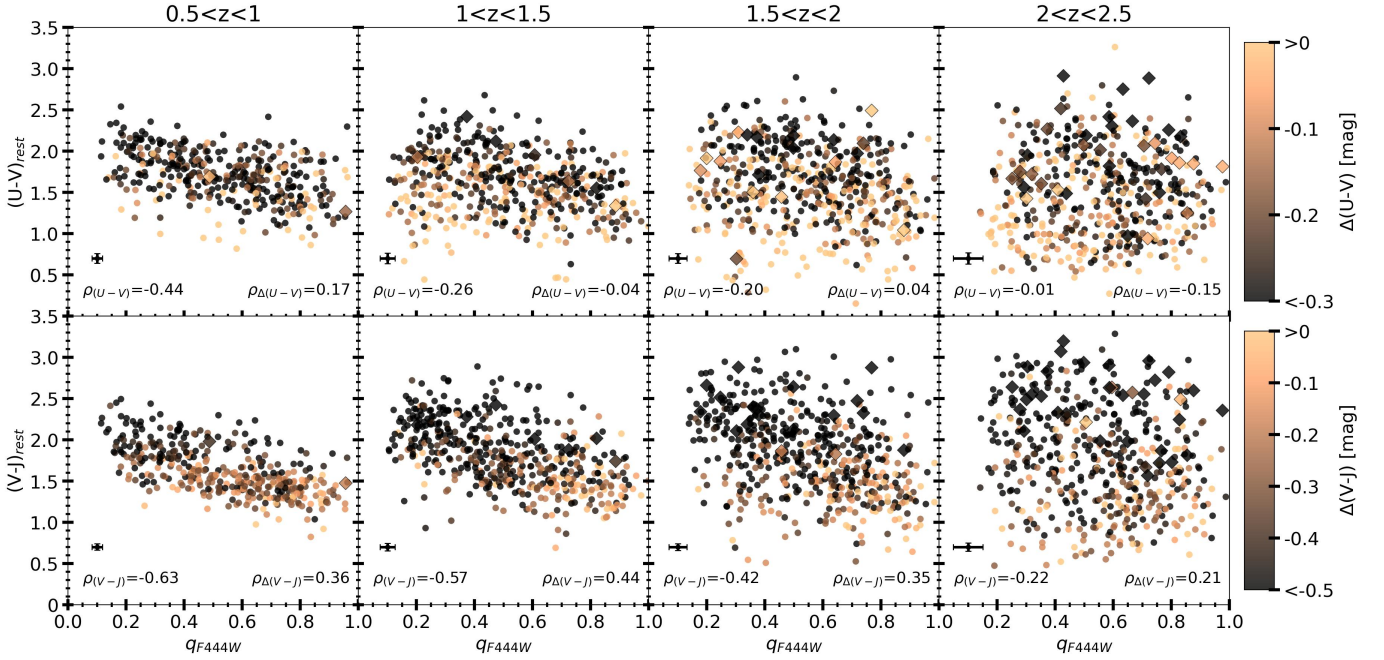


Fig. 8. Same as Figure 7 but for $M_\star \geq 10^{10.5} M_\odot$ star-forming galaxies. Diamonds identify sub-mm-selected galaxies. The correlation between the colors and q decreases with redshift.

tion with redshift we now consider the connection between axis ratio, as a proxy for viewing angle and attenuation properties (as traced by colors and color gradients) for quiescent and star-forming galaxies with $M_\star > 10^{10.5} M_\odot$. The motivation for this mass selection is that those star-forming galaxies are most likely to be disk-like in both a geometric sense (oblate and flattened van der Wel et al. 2014; Zhang et al. 2019) and as expressed

by their kinematic properties (e.g., Förster Schreiber et al. 2009; Wisnioski et al. 2015).

For disks (flat oblates), the projected axis ratio q , as measured in the F444W filter by the two-dimensional Sérsic light profile fit, is a good tracer of the inclination, that is, a one-dimensional viewing angle. In Figure 7 and 8 we show the distribution of q and the global $U - V$ and $V - J$ colors in bins of redshift for the quiescent and star-forming population respectively.

For the population of quiescent galaxies, little correlation between color and axis ratio q is expected (as suggested by their tight color sequences, see van der Wel et al. 2025, and confirmed by the low Spearman correlation coefficients reported in the bottom left corner of each panel of Fig. 7). Many, if not most, of these galaxies are shaped like oblate disks (Chang et al. 2013) up to at least $z = 2$. The absence of a correlation with q then implies that color is independent of inclination, which we interpret as evidence for transparency, that is, small dust columns. This is in line with the recent result that even quiescent galaxies with significant molecular gas reservoirs do not have much dust (Spilker et al. 2025). Changing the definition of the quiescent boundary in the UVJ diagram adopted in this work – now set to $V - J < 1.5$ (Muzzin et al. 2013) – does not alter the conclusions drawn on the basis of Fig. 7. Further investigation of dust in quiescent galaxies requires a selection based on the sSFR (possibly retrieved from non-parametric SED fitting including far-IR photometry) to avoid any color-selection systematic.

Conversely, for star-forming galaxies at $z < 1.5$ the trend is familiar and expected: flat (edge-on) galaxies are redder than round (face-on) galaxies. The connection between color and viewing angle (well traced by the axis ratio for low- z star-forming galaxies, see e.g., van der Wel et al. 2014) was previously established at $z \approx 1$ by (Patel et al. 2012). The small scatter in color at fixed q (0.2 mag in $V - J$) is also noteworthy: variation among the galaxies in terms of their intrinsic properties (star-formation, stellar population, dust content) must be relatively small and to a large extent the observed colors are determined by inclination. We also see a correlation between color gradient and axis ratio: face-on galaxies (large q) have weaker gradients than edge-on (low q) galaxies (Spearman correlation coefficient $\rho_{(U-V)} \approx -0.3$ and $\rho_{(V-J)} \approx -0.6$). In edge-on galaxies, the dust obscures the central region more than the outer parts. This correlation is weaker than the q -color correlation, but still significant, especially for $\Delta(V - J)$ (in fact, $\rho_{\Delta(U-V)} \approx 0.1$ and $\rho_{\Delta(V-J)} \approx 0.4$). Taking these trends together, we arrive at a picture that is consistent with the result that massive present-day spiral galaxies (with $V_c > 120 \text{ km s}^{-1}$; $M_\star \gtrsim 10^{10} M_\odot$) show thin, smooth, regular and galaxy-wide dust lanes aligned with the gravitationally dominant stellar disk (Dalcanton et al. 2004).

But at $z > 1.5$ the trends change and the correlations between q and colors / color gradients weaken (with $\rho_{(U-V)}$ that drops to ~ -0.1 and $\rho_{(V-J)}$ to ≈ -0.2). Viewing angle no longer matters in the same manner as at later cosmic times. To some extent, this is due to the less obviously disk-like nature of at least a subset of the galaxies. Rotational support decreases with redshift (Kassin et al. 2012; Wisnioski et al. 2015; Übler et al. 2019), and the distribution of geometries is more varied (van der Wel et al. 2014; Zhang et al. 2019) so that axis ratio no longer tracks viewing angle in a unique manner. But the disappearance of disks is not the full story: a large fraction of galaxies is still disk-like in nature, the evidence for which was recently bolstered by the large observed fraction of galaxies with spiral arms in this mass and redshift range (e.g., Espejo Salcedo et al. 2025, found 72% of the galaxies with $2 < z < 2.5$ to be disk-like and 20% to host spiral arms), the existence of which are only possible in relatively thin stellar and/or gaseous disks.

Yet the fact remains that the correlations between q and the color (gradient) information are less obvious in statistical terms and less straightforward to interpret. At $z > 2$ the $q - (V - J)$ correlation is still significant ($\rho_{(V-J)} = -0.22$), but weaker than at $z < 1.5$, and with a very clear increase in scatter at fixed q (0.7 mag at $z > 2$ compared to 0.2 mag at $z < 1$). Likewise, the $q - \Delta(V - J)$ correlation persists at $z > 2$ ($\rho_{\Delta(V-J)} = 0.21$), if slightly

weaker, with stronger gradients for flat (edge-on) galaxies. For $U - V$ the picture is different from $V - J$.

At $z > 2$ there is no $q - (U - V)$ correlation ($\rho_{(U-V)} \approx 0$), and, if anything, a weak anti-correlation between q and $\Delta(U - V)$ ($\rho_{\Delta(U-V)} = -0.15$), with slightly stronger gradients in round (face-on) galaxies. This trend is driven by a population of galaxies with blue integrated $U - V$ colors, weak $U - V$ gradients, but red $V - J$ colors and strong $V - J$ gradients. This population is already apparent at $1 < z < 1.5$, and a prototypical example is shown in the center of the 3×3 set of panels in Figure 3. The $U - V$ trends are explained by a patchy but not clearly radially varying distribution of relatively unobscured star-formation across the side of the underlying disk that is pointed in the direction of the observer.

Taken together, these color and color gradient trends with q clearly show that the dust-to-star geometry at $z > 1.5$ is fundamentally different from the thin, regular dust-lane geometry seen at $0 < z < 1.5$. The evidence suggests that the dust distribution still retains some of the axisymmetric characteristics of a dust lane, given the bluer colors of face-on galaxies. But the much larger A_V values also imply that the dust lane must be more vertically extended, looking more like a patchy thick disk, obscuring the majority of all intrinsic rest-frame V -band light. Such a thick disk of dust must also be centrally concentrated, as implied by the color gradients, which are stronger for edge-on, high- A_V galaxies (see correlation coefficients in Figure 8). Finally, the dust distribution is also less smooth and regular than their thin present-day counterparts, as indicated by the large scatter in the $U - V$ and $V - J$ colors and their gradients. This dust model closely matches the one discussed in the rightmost panel of Fig. 7 of Gebek et al. (2025).

4. Conclusions

In this paper we used the combination of HST and JWST imaging to quantify and examine gradients in rest frame $U - V$ and $V - J$ colors for over 10, 200 galaxies at redshifts $0.5 < z < 2.5$ with stellar masses $M_\star > 10^{9.5} M_\odot$. To stabilize our color measurements against issues related to background subtraction and the PSF, we perform multi-wavelength 2D brightness modeling that fits a Sérsic profile to each galaxy at each observed wavelength. We then measure the colors from these Sérsic profiles.

$U - V$ color gradients in star-forming galaxies (Fig. 5) show a mild stellar mass dependence – with stronger gradients for more massive galaxies – and a weak redshift evolution. Their $V - J$ color gradients, on the other hand, are strongly mass and redshift dependent, with high-mass $2 < z < 2.5$ galaxies showing the strongest gradients on average. The central regions, in particular, have much redder $V - J$ colors than can be explained by any dust-free stellar population. This, in combination with the strong link between $V - J$ gradient and global A_V we find, suggests that the optical and near-IR colors of high mass galaxies reflect a strong attenuation gradient and highly obscured centers. Together with stellar population gradients, strong dust gradients produce $U - V$ and $V - J$ gradients that systematically shift the galaxy population within the UVJ color plane. Finally, the strongest gradients and reddest colors are seen for edge-on galaxies at $z > 1.5$. The high A_V values imply a vertically extended dust geometry in the plane of the stellar disk, rather than the thin dust lanes seen at lower z .

Meanwhile, the quiescent galaxy population has negative radial gradients in both $U - V$ and $V - J$ colors, with little or no redshift evolution. The lack of a relation between viewing angle/inclination and color implies that these galaxies are

largely transparent and, in line with our knowledge of gradients in present-day early-type galaxies, that the color gradients are the result of stellar population gradients. The lack of a redshift evolution in the strength of the gradient may be the result of weakening age-induced gradients with cosmic time that are compensated for by increasing metallicity gradients, but further study is needed to confirm this picture.

The results of this work serve as a benchmark for the examination of the origin of gradients in cosmological simulations (e.g., Donnari et al. 2019; Akins et al. 2022; Gebek et al. 2025), to help understand the dust geometry and structure of galaxies 10 Gyr ago.

Acknowledgements. MM acknowledges the financial support of the Flemish Fund for Scientific Research (FWO-Vlaanderen), research project G030319N. (Some of) The data products presented herein were retrieved from the Dawn JWST Archive (DJA). DJA is an initiative of the Cosmic Dawn Center (DAWN), which is funded by the Danish National Research Foundation under grant DNR140.

References

- Adscheid, S., Magnelli, B., Liu, D., et al. 2024, *A&A*, 685, A1
- Akins, H. B., Narayanan, D., Whitaker, K. E., et al. 2022, *ApJ*, 929, 94
- Barbary, K. 2016, *Journal of Open Source Software*, 1, 58
- Barišić, I., Pacifici, C., van der Wel, A., et al. 2020, *ApJ*, 903, 146
- Belfiore, F., Maiolino, R., Bundy, K., et al. 2018, *MNRAS*, 477, 3014
- Belfiore, F., Maiolino, R., Maraston, C., et al. 2017, *MNRAS*, 466, 2570
- Bell, E. F. & de Jong, R. S. 2000, *MNRAS*, 312, 497
- Belli, S., Newman, A. B., & Ellis, R. S. 2019, *ApJ*, 874, 17
- Benton, C. E., Nelson, E. J., Miller, T. B., et al. 2024, *ApJ*, 974, L28
- Bertin, E. & Arnouts, S. 1996, *A&AS*, 117, 393
- Brammer, G. B., van Dokkum, P. G., & Coppi, P. 2008, *ApJ*, 686, 1503
- Brammer, G. B., Whitaker, K. E., van Dokkum, P. G., et al. 2011, *ApJ*, 739, 24
- Byrne, C. M., Stanway, E. R., Eldridge, J. J., McSwiney, L., & Townsend, O. T. 2022, *MNRAS*, 512, 5329
- Carnall, A. C., McLure, R. J., Dunlop, J. S., et al. 2023, *Nature*, 619, 716
- Casey, C. M., Kartaltepe, J. S., Drakos, N. E., et al. 2023, *ApJ*, 954, 31
- Chabrier, G. 2003, *PASP*, 115, 763
- Chang, Y.-Y., van der Wel, A., Rix, H.-W., et al. 2013, *ApJ*, 773, 149
- Chapman, S. C., Windhorst, R., Odewahn, S., Yan, H., & Conselice, C. 2003, *ApJ*, 599, 92
- Clausen, M., Momcheva, I. G., Whitaker, K. E., et al. 2025, *ApJ*, 993, 106
- Conroy, C. & Gunn, J. E. 2010, *ApJ*, 712, 833
- Conroy, C., Gunn, J. E., & White, M. 2009, *ApJ*, 699, 486
- Cullen, F., McLure, R. J., Khochfar, S., et al. 2018, *MNRAS*, 476, 3218
- Cutler, S. E., Whitaker, K. E., Weaver, J. R., et al. 2024, *ApJ*, 967, L23
- Daddi, E., Cimatti, A., Renzini, A., et al. 2004, *ApJ*, 600, L127
- Daddi, E., Dickinson, M., Morrison, G., et al. 2007, *ApJ*, 670, 156
- Dalcanton, J. J., Yoachim, P., & Bernstein, R. A. 2004, *ApJ*, 608, 189
- de Jong, R. S. 1996, *A&A*, 313, 45
- Donnari, M., Pillepich, A., Nelson, D., et al. 2019, *MNRAS*, 485, 4817
- Dunlop, J. S., Abraham, R. G., Ashby, M. L. N., et al. 2021, *PRIMER: Public Release IMaging for Extragalactic Research*, JWST Proposal. Cycle 1, ID. #1837
- Dutton, A. A., van den Bosch, F. C., Faber, S. M., et al. 2011, *MNRAS*, 410, 1660
- Eisenstein, D. J., Willott, C., Alberts, S., et al. 2023, *arXiv e-prints*, [arXiv:2306.02465](https://arxiv.org/abs/2306.02465)
- Ellison, S. L., Sánchez, S. F., Ibarra-Medel, H., et al. 2018, *MNRAS*, 474, 2039
- Espejo Salcedo, J. M., Pastras, S., Vácha, J., et al. 2025, *A&A*, 700, A42
- Finkelstein, S. L., Bagley, M. B., Ferguson, H. C., et al. 2023, *ApJ*, 946, L13
- Finkelstein, S. L., Dickinson, M., Ferguson, H. C., et al. 2017, *The Cosmic Evolution Early Release Science (CEERS) Survey*, JWST Proposal ID 1345. Cycle 0 Early Release Science
- Förster Schreiber, N. M., Genzel, R., Bouché, N., et al. 2009, *ApJ*, 706, 1364
- Franx, M., Labbé, I., Rudnick, G., et al. 2003, *ApJ*, 587, L79
- Gebek, A., Diemer, B., Martorano, M., et al. 2025, *A&A*, 695, A90
- Gillman, S., Smail, I., Gullberg, B., et al. 2024, *A&A*, 691, A299
- Goddard, D., Thomas, D., Maraston, C., et al. 2017, *MNRAS*, 466, 4731
- Greener, M. J., Aragón-Salamanca, A., Merrifield, M. R., et al. 2020, *MNRAS*, 495, 2305
- Grogin, N. A., Kocevski, D. D., Faber, S. M., et al. 2011, *ApJS*, 197, 35
- Guo, Y., Giallisco, M., Cassata, P., et al. 2011, *ApJ*, 735, 18
- Häußler, B., Bamford, S. P., Vika, M., et al. 2013, *MNRAS*, 430, 330
- Hinkley, S. & Im, M. 2001, *ApJ*, 560, L41
- Hodge, J. A., Swinbank, A. M., Simpson, J. M., et al. 2016, *ApJ*, 833, 103
- Ito, K., Valentino, F., Brammer, G., et al. 2024, *ApJ*, 964, 192
- Jones, A. P., Köhler, M., Ysard, N., Bocchio, M., & Verstraete, L. 2017, *A&A*, 602, A46
- Kassin, S. A., Weiner, B. J., Faber, S. M., et al. 2012, *ApJ*, 758, 106
- Kelvin, L. S., Driver, S. P., Robotham, A. S. G., et al. 2012, *MNRAS*, 421, 1007
- Kennedy, R., Bamford, S. P., Baldry, I., et al. 2015, *MNRAS*, 454, 806
- Killi, M., Watson, D., Brammer, G., et al. 2024, *A&A*, 691, A52
- Koekemoer, A. M., Faber, S. M., Ferguson, H. C., et al. 2011, *ApJS*, 197, 36
- Kriek, M. & Conroy, C. 2013, *ApJ*, 775, L16
- La Barbera, F. & de Carvalho, R. R. 2009, *ApJ*, 699, L76
- Labbé, I., Huang, J., Franx, M., et al. 2005, *ApJ*, 624, L81
- Le Bail, A., Daddi, E., Elbaz, D., et al. 2024, *A&A*, 688, A53
- Leja, J., Speagle, J. S., Ting, Y.-S., et al. 2022, *ApJ*, 936, 165
- Lin, L., Belfiore, F., Pan, H.-A., et al. 2017, *ApJ*, 851, 18
- Lin, L., Hsieh, B.-C., Pan, H.-A., et al. 2019, *ApJ*, 872, 50
- Lin, L., Shen, S., Yesuf, H. M., Mao, Y.-W., & Hao, L. 2024, *ApJ*, 977, 175
- Liu, F. S., Jiang, D., Faber, S. M., et al. 2017, *ApJ*, 844, L2
- Liu, F. S., Jiang, D., Guo, Y., et al. 2016, *ApJ*, 822, L25
- Lorenz, B., Kriek, M., Shapley, A. E., et al. 2024, *ApJ*, 975, 187
- Maheson, G., Tacchella, S., Belli, S., et al. 2025, *arXiv e-prints*, [arXiv:2504.15346](https://arxiv.org/abs/2504.15346)
- Martorano, M., van der Wel, A., Baes, M., et al. 2025, *A&A*, 694, A76
- Martorano, M., van der Wel, A., Baes, M., et al. 2024, *ApJ*, 972, 134
- Martorano, M., van der Wel, A., Bell, E. F., et al. 2023, *ApJ*, 957, 46
- McGrath, E. J., Stockton, A., Canalizo, G., Iye, M., & Maihara, T. 2008, *ApJ*, 682, 303
- Menanteau, F., Abraham, R. G., & Ellis, R. S. 2001, *MNRAS*, 322, 1
- Miller, T. B., van Dokkum, P., & Mowla, L. 2023, *ApJ*, 945, 155
- Miller, T. B., Whitaker, K. E., Nelson, E. J., et al. 2022, *ApJ*, 941, L37
- Mosleh, M., Hosseini, S., Hosseini-Shahi-Savandi, S. Z., & Tacchella, S. 2020, *ApJ*, 905, 170
- Mosleh, M., Tacchella, S., Renzini, A., et al. 2017, *ApJ*, 837, 2
- Muzzin, A., Marchesini, D., Stefanon, M., et al. 2013, *ApJ*, 777, 18
- Nedkova, K. V., Rafelski, M., Teplitz, H. I., et al. 2024, *ApJ*, 970, 188
- Nelson, E. J., Tadaki, K.-i., Tacconi, L. J., et al. 2019, *ApJ*, 870, 130
- Nelson, E. J., van Dokkum, P. G., Momcheva, I. G., et al. 2016, *ApJ*, 817, L9
- Nersesian, A., van der Wel, A., Gallazzi, A. R., et al. 2025, *A&A*, 695, A86
- Ng, P. & Maechler, M. 2007, *Statistical Modelling*, 7, 315
- Ng, P. & Maechler, M. 2022, *COBS – Constrained B-splines (Sparse matrix based)*, r package version 1.3-5.
- Oesch, P. A., Brammer, G., Naidu, R. P., et al. 2023, *MNRAS*, 525, 2864
- Oke, J. B. & Gunn, J. E. 1983, *ApJ*, 266, 713
- Ormerod, K., Conselice, C. J., Adams, N. J., et al. 2024, *MNRAS*, 527, 6110
- Patel, S. G., Holden, B. P., Kelson, D. D., et al. 2012, *ApJ*, 748, L27
- Peletier, R. F., Davies, R. L., Illingworth, G. D., Davis, L. E., & Cawson, M. 1990, *AJ*, 100, 1091
- Peng, C. Y., Ho, L. C., Impey, C. D., & Rix, H.-W. 2002, *AJ*, 124, 266
- Peng, C. Y., Ho, L. C., Impey, C. D., & Rix, H.-W. 2010, *AJ*, 139, 2097
- Perrin, M. D., Sivaramakrishnan, A., Lajoie, C.-P., et al. 2014, in *Society of Photo-Optical Instrumentation Engineers (SPIE) Conference Series*, Vol. 9143, *Space Telescopes and Instrumentation 2014: Optical, Infrared, and Millimeter Wave*, ed. J. Oschmann, Jacobus M., M. Clampin, G. G. Fazio, & H. A. MacEwen, 91433X
- Price, S. H., Kriek, M., Brammer, G. B., et al. 2014, *ApJ*, 788, 86
- Price, S. H., Suess, K. A., Williams, C. C., et al. 2025, *ApJ*, 980, 11
- Ren, J., Liu, F. S., Li, N., et al. 2025, *ApJ*, 982, 200
- Salim, S., Boquien, M., & Lee, J. C. 2018, *ApJ*, 859, 11
- Sánchez-Blázquez, P., Rosales-Ortega, F. F., Méndez-Abreu, J., et al. 2014, *A&A*, 570, A6
- Sandage, A. 1972, *ApJ*, 176, 21
- Shirley, R., Roehlly, Y., Hurley, P. D., et al. 2019, *MNRAS*, 490, 634
- Smail, I., Ivison, R. J., & Blain, A. W. 1997, *ApJ*, 490, L5
- Smail, I., Ivison, R. J., Blain, A. W., & Kneib, J. P. 2002, *MNRAS*, 331, 495
- Spilker, J. S., Whitaker, K. E., Narayanan, D., et al. 2025, *ApJ*, 993, L40
- Suess, K. A., Bezanson, R., Nelson, E. J., et al. 2022, *ApJ*, 937, L33
- Suess, K. A., Kriek, M., Price, S. H., & Barro, G. 2019a, *ApJ*, 877, 103
- Suess, K. A., Kriek, M., Price, S. H., & Barro, G. 2019b, *ApJ*, 885, L22
- Suess, K. A., Kriek, M., Price, S. H., & Barro, G. 2020, *ApJ*, 899, L26
- Szomoru, D., Franx, M., van Dokkum, P. G., et al. 2010, *ApJ*, 714, L244
- Szomoru, D., Franx, M., van Dokkum, P. G., et al. 2013, *ApJ*, 763, 73
- Tacchella, S., Carollo, C. M., Förster Schreiber, N. M., et al. 2018, *ApJ*, 859, 56
- Tacchella, S., Dekel, A., Carollo, C. M., et al. 2016, *MNRAS*, 458, 242
- Tadaki, K.-i., Belli, S., Burkert, A., et al. 2020, *ApJ*, 901, 74
- Tadaki, K.-i., Genzel, R., Kodama, T., et al. 2017, *ApJ*, 834, 135
- Tan, Q.-H., Daddi, E., Magnelli, B., et al. 2024, *Nature*, 636, 69
- Tortora, C., Napolitano, N. R., Cardone, V. F., et al. 2010, *MNRAS*, 407, 144
- Tortora, C., Napolitano, N. R., Romanowsky, A. J., et al. 2011, *MNRAS*, 418, 1557

- Übler, H., Genzel, R., Wisnioski, E., et al. 2019, *ApJ*, 880, 48
- Valentino, F., Brammer, G., Gould, K. M. L., et al. 2023, *ApJ*, 947, 20
- van der Wel, A., Chang, Y.-Y., Bell, E. F., et al. 2014, *ApJ*, 792, L6
- van der Wel, A., Martorano, M., Häußler, B., et al. 2024, *ApJ*, 960, 53
- van der Wel, A., Martorano, M., Marchesini, D., et al. 2025, *A&A*, 701, A30
- Vika, M., Bamford, S. P., Häußler, B., et al. 2013, *MNRAS*, 435, 623
- Wang, W., Faber, S. M., Liu, F. S., et al. 2017, *MNRAS*, 469, 4063
- Williams, C. C., Oesch, P. A., Weibel, A., et al. 2025, *ApJ*, 979, 140
- Williams, C. C., Tacchella, S., Maseda, M. V., et al. 2023, *ApJS*, 268, 64
- Wisnioski, E., Förster Schreiber, N. M., Wuyts, S., et al. 2015, *ApJ*, 799, 209
- Wu, H., Shao, Z., Mo, H. J., Xia, X., & Deng, Z. 2005, *ApJ*, 622, 244
- Wuyts, S. & Förster Schreiber, N. M. 2020, in *IAU Symposium*, Vol. 352, *Uncovering Early Galaxy Evolution in the ALMA and JWST Era*, ed. E. da Cunha, J. Hodge, J. Afonso, L. Pentericci, & D. Sobral, 253–265
- Wuyts, S., Förster Schreiber, N. M., Genzel, R., et al. 2012, *ApJ*, 753, 114
- Wuyts, S., Förster Schreiber, N. M., Nelson, E. J., et al. 2013, *ApJ*, 779, 135
- Wuyts, S., Labbé, I., Franx, M., et al. 2007, *ApJ*, 655, 51
- Zhang, H., Primack, J. R., Faber, S. M., et al. 2019, *MNRAS*, 484, 5170
- Zibetti, S. & Gallazzi, A. R. 2022, *MNRAS*, 512, 1415

Appendix A: Effect of residual flux on the measured color gradients

The color gradients investigated in this paper are computed based on the single Sérsic profiles from GalfitM, without a residual correction as first employed by Szomoru et al. (2010). In this appendix, we verify the impact of the residuals on the retrieved colors. We measured the residual fluxes within $R_{e,F444W}$ and between $1 - 2R_{e,F444W}$ for three filters (F115W, F150W and F356W), which approximately cover the U , V , and J bands at $z = 2$. We then compute F115W–F150W and F150W–F356W colors from the Sérsic profiles (S) and from the Sérsic profiles plus the fit residuals (S+R). The difference between S+R color and S color is shown in Figure A.1 as a function of A_V and color-coded with the redshift. The median difference between colors measured within R_e and between $1 - 2R_{e,F444W}$ is negligible, with a maximum standard deviation of 0.03 mag. The maximum standard deviation occurs for colors measured in the core of galaxies, where residual corrections are sensitive to errors in the PSF model. The 16-84 percentile range is increased for highly attenuated galaxies, for which the gradient estimates are also the most uncertain due to the small flux in F115W: the effect of the residuals is comparable with the uncertainties. Concerning the outer annuli (bottom row of the figure), we see that the residuals play no significant role, with only a mild increase in scatter for high A_V in the color F115W–F150W. We find no significant dependence on redshift or stellar mass.

We note that for individual images the residuals are larger than for the colors: the covariance between the residuals in different filters reduces the impact on our color gradient estimates. Since residual corrections are very small (Fig. A.1) and can introduce new errors (PSF uncertainties affect the centers; noise peaks affect the low surface brightness outer parts), we choose to omit the residual corrections in this paper.

Appendix B: Estimate of the color gradient's uncertainties

Color gradients presented in this work are computed by retrieving rest-frame U , V , J fluxes via SED fitting with the code EAZY. Random uncertainties are given by a combination of the observed flux uncertainties and model uncertainties - the underlying SED. Uncertainties provided by EAZY on the rest-frame fluxes include both. When computing color gradients, the covariant terms of the uncertainty on each band's flux cancel out with the net effect that the final uncertainty is expected to be smaller than the simple quadrature sum of the uncertainties of all fluxes involved in the color gradient. In fact, covariant terms originate from the SED model, which affects the same way rest-frame fluxes computed at a fixed aperture. On the other hand, uncertainties on color gradients computed from observed fluxes are just given by the quadrature sum of the uncertainties on all the fluxes involved since no convolution with an SED model is involved in their determination.

To estimate the true uncertainty on color gradients, we compared the color gradients derived using rest-frame colors from EAZY (the same used throughout the paper) with color gradients computed using observed fluxes in the filters closest to the rest-frame bands investigated. The total scatter of the former (σ_{EAZY}^2) can be written as

$$\sigma_{EAZY}^2 = \sigma_{flux}^2 + \sigma_{covariant}^2 \quad (B.1)$$

The constraint set in Section 2.3 that observations must overlap at least 50% of the rest-frame bands, combined with the state-

ments of Brammer et al. (2011) who found colors retrieved with EAZY to accurately match colors retrieved by interpolating fluxes in nearby observed bands (when these overlap sufficiently with the rest-frame band), makes any bandpass mismatch errors negligible. The total scatter of the second (σ_{OBS}^2) can be written as

$$\sigma_{OBS}^2 = \sigma_{flux}^2 + \sigma_{\lambda}^2 \quad (B.2)$$

with σ_{flux}^2 the scatter due to flux uncertainties, $\sigma_{covariant}^2$ the scatter due to covariance terms and σ_{λ}^2 the scatter due to the difference in band coverage between the rest-frame band investigated and the closest filter. Since the sample is selected such that at least 50% of the area of the rest-frame band overlaps with observations, the scatter due to this term can be considered negligible compared to the others.

The scatter in the comparison between the two color gradients is then representative of the covariant term. Hence, the real uncertainty on EAZY color gradients used in this work can be computed as $\sigma_{ColorGrad} = \sqrt{\sigma_{OBS}^2 + \sigma_{covariant}^2(z)}$ where the latter term is represented by the scatter in Figure B.1 and is expressed as a function of redshift.

To account also for the uncertainties of R_e on the color gradients, we add in quadrature to $\sigma_{ColorGrad}$ a new term σ_{Sersic} computed as the ratio between the fraction of light enclosed in the Sérsic profile tracing the U band up to $R_{e,V}$ that is the effective radius measured in the V band. The same is done for the V and J bands. This term accounts for the uncertainty induced by retrieving photometry from several different modeled Sérsic profiles and has a median value of $\sigma_{Sersic,U-V} \approx 0.07$ mag and $\sigma_{Sersic,V-J} \approx 0.09$ mag, comparable or smaller than the scatter shown in Figure B.1.

Appendix C: Color gradients and the wavelength dependence of size

A color gradient and a size difference measured at different wavelengths are (nearly) the same thing, especially when both derive from the same light profile fits. In fact, such size differences are often referred to as color gradients (i.e., Suess et al. 2022; Cutler et al. 2024; Ito et al. 2024; Ormerod et al. 2024; Martorano et al. 2024; Clausen et al. 2025). Specifically, in our previous work Martorano et al. (2024), we found a median optical-to-near-IR size ratio of 0.14 dex, and up to 0.25 dex for massive star-forming galaxies at $z > 1.5$. These results precisely mirror the color gradient trends analyzed in this paper, which aims at interpreting the origin of the color gradients (attenuation) rather than its effect on the measured structural evolution of galaxies. It is still useful to compare the color gradients, in this paper defined as the color difference between the outskirts (1 and $2R_e$) and the center (inside R_e), with the size difference between the optical (rest-frame $0.5 \mu\text{m}$) and near-IR (rest-frame $1.5 \mu\text{m}$) from Martorano et al. (2024), even if both derive from the same Sérsic profile fits. In Figure C.1 we compare, for star-forming galaxies, the size differences with the $V - J$ color gradients.

There exists a strong correlation between the stellar mass and the size variation: low-mass galaxies have a median size variation of $\approx 25\%$ while massive galaxies have median variations of $\approx 65\%$, as presented in Martorano et al. (2024). No clear redshift trend is recovered for any of the stellar mass bin investigated. By construction, this size difference closely correlates with our $\Delta(V - J)$, but there is substantial scatter that originates from variations in Sérsic index, that is the distribution of light within the two large apertures used to define the color gradient. A larger

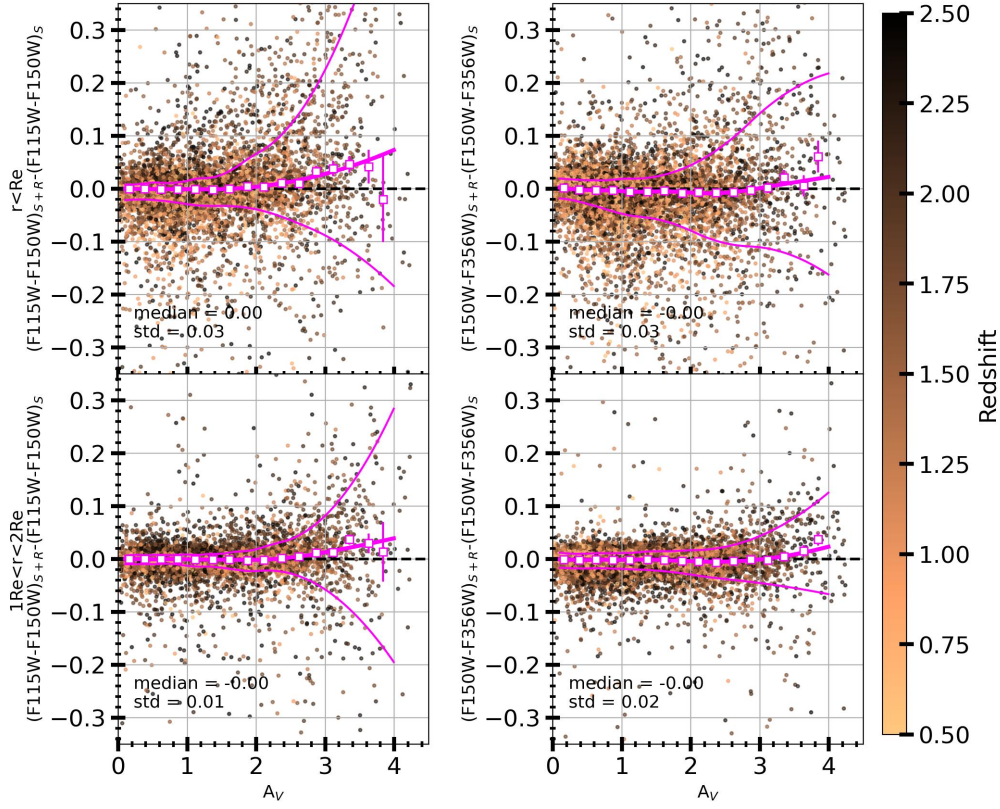


Fig. A.1. Difference between the flux difference (i.e. color gradient) between F115W–F150W (first column) and F150W–F356W (second column) computed using photometry from the Sérsic profile adding back the fit residuals (S+R) or just from the Sérsic profiles (S) measured within the effective radius $R_{e,F444W}$ (first row) or between $1 - 2 R_{e,F444W}$ (second row). These are presented as a function of the global A_V and color-coded with the galaxy redshift. White squares with magenta contour show the median difference in A_V bins of width 0.2 mag, while error bars show the statistical uncertainty (σ/\sqrt{N}). Solid magenta lines show the 16-50-84 percentiles computed with the cobs library (Ng & Maechler 2007, 2022), which allows for a smoothed combination of a spline regression and quantile regression. In the bottom left corner of each panel we report the median color difference and the standard deviation.

Sérsic index produces a larger size difference at a fixed color gradient (top row in Figure C.1). In addition, if the Sérsic index varies with wavelength (i.e., Kelvin et al. 2012; Vika et al. 2013; Kennedy et al. 2015; Martorano et al. 2023, 2025), then galaxies with strong color gradients may show just a mild difference in size and, vice versa, galaxies with mild color gradients may show strong size gradients (lower row in Figure C.1). The take-away message is that radial variations in color do not necessarily lead to net color gradient expressed as a summary statistic (here, comparing the average color between 1 and $2 R_e$ with that inside R_e as measured in F444W). Conversely, the lack of a color gradient as defined here, does not necessarily imply that the color is the same at all radii. The lack of a clear redshift trend in this figure proves that the size variation as a function of redshift presented in Martorano et al. (2024) is comparable to that presented in this work.

Sub-mm galaxies in our sample exhibit both strong color gradients and size variations (confirming results presented in Ren et al. 2025) that closely align with the median trends. These galaxies have median $n_{1.5\mu m} \sim 1.3$ and $n_{0.5\mu m} \sim 1.1$ confirming findings of Price et al. (2025); Gillman et al. (2024) and several others. As in Price et al. (2025), we find more concentrated sub-mm galaxies to have stronger size variation, suggesting galaxies with the most compact light distributions also have the most concentrated dust.

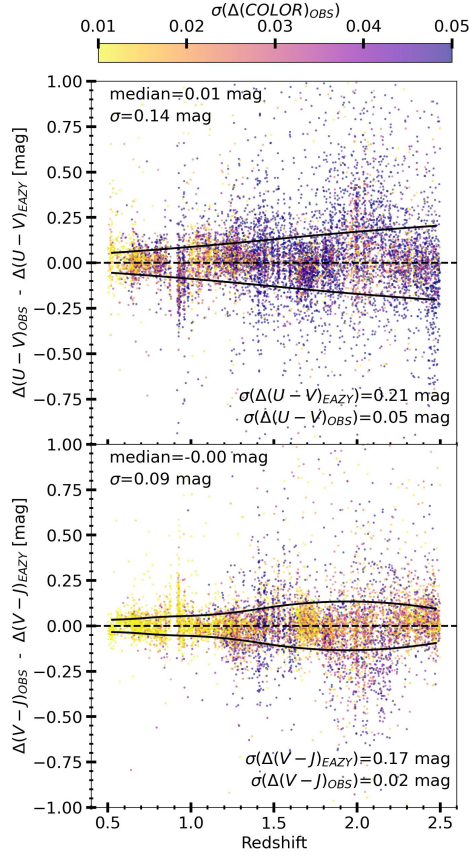


Fig. B.1. Comparison between the color gradients retrieved with EAZY rest-frame fluxes and observed fluxes as a function of redshift and color coded with the uncertainty on the color gradient retrieved using observed fluxes. The top panel shows the $U - V$ color difference, while the bottom panel shows the $V - J$ color difference. In the top left corner of each panel we present the median and standard deviation of the color gradient difference, while in the bottom right corner we show the median uncertainty on the two color gradients. Solid black lines show the standard deviation of the difference between the two color gradients as a function of redshift.

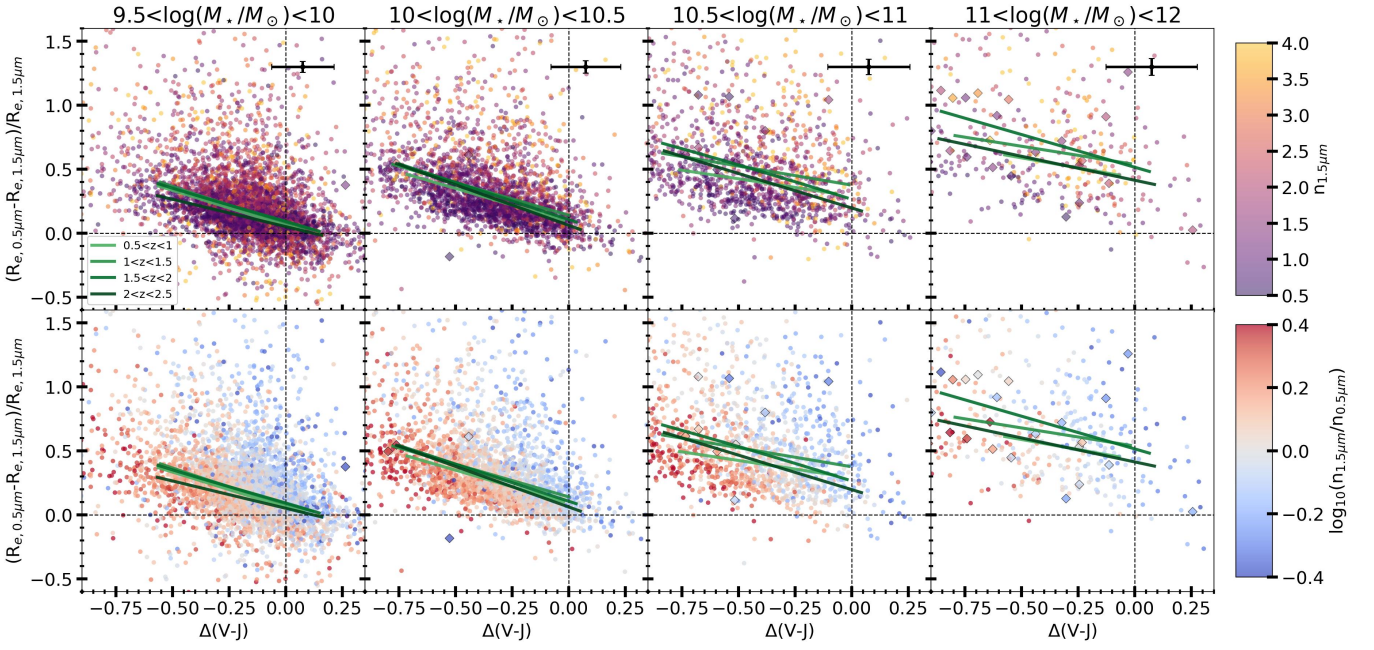


Fig. C.1. $V-J$ color gradient vs relative size variation in four stellar mass bins. The two rows show the same data but color-coded respectively with the Sérsic index at $1.5\,\mu\text{m}$ (top row) and the logarithm difference of Sérsic indices at rest-frame $1.5\,\mu\text{m}$ and $0.5\,\mu\text{m}$ (lower row). Just star-forming galaxies are shown. Diamonds show sub-mm-selected galaxies and are color-coded following the same color scheme of the other galaxies. Colored green lines show the running median in redshift bins. In the top right corner, we present the median uncertainties. Massive star-forming galaxies have systematically stronger size variation with wavelength and stronger color gradients than low-mass galaxies. The variation of the Sérsic index with wavelength correlates more strongly with the color gradient than with the size gradient.